Article

MMS

Mathematics and Mechanics of Solids
1–12

DOI: 10.1177/10812865211011217
journals.sagepub.com/home/mms
SAGE

DEM modeling and simulation of post-impact shotgun pellet ricochet for safety analysis

Tarek I. Zohdi
Department of Mechanical Engineering, University of California, Berkeley, CA, USA

Received 20 January 2021; accepted 31 March 2021

Abstract
Shotguns have increasingly used case-hardened steel pellets, as opposed to "classical" lead, owing to food safety and environmental concerns. Correspondingly, there is increasing concern about unintended ricochet of pellets and subsequent bodily harm, such as eye damage. Correspondingly, this paper focuses on the impact of pellets with a surface and the post-impact ricochet range. Equations for general three-dimensional inelastic impact with unilateral stick–slip conditions are derived for pellets and a post-impact trajectory analysis is performed. Qualitatively, with increasing friction, ranges of ricochet decrease because most of the pre-impact translational energy of the pellets is converted upon impact into rotational energy, which reduces the post-impact ricochet range. For slippery surfaces, wide ranging trajectory distributions occur owing to the mix of stick and slip conditions among the pellets. In the case of slip, the pellets retain much of their translational energy and the post-impact linear velocities are greater than high-friction cases, which leads to much larger post-impact trajectory ranges. The model enables analysts to make more quantitative decisions on the choices of parameters associated with shotgun use and can reduce trial-and-error procedures in testing.

Keywords
Shotgun, ricochet, simulation, safety

1. Introduction

Worldwide, there is extensive use of shotguns for hunting, target practice, etc. A shotgun shell is used to house the pellets before firing, and usually consists of a plastic or paper tube mounted on a brass cylinder that holds the powder (Figure 1). A wad is placed over the powder to avoid mixing the pellets and powder, and to provide a seal so that the expanding gas does not blow through the pellets. While, historically, lead was used for pellets, environmental (lead toxicity) safety concerns has reduced its usage. In the mid 1950s, there was a push towards phasing out lead shot. By the 1970s, the US Fish and Wildlife Service designated exclusively steel shot for waterfowl hunting. Shot pellets are usually made by cutting wrought carbon steel wire and rolling the bits into hard spheres.[1] Smooth hard spheres (pellets) are used, because they do not usually break owing to their case-hardened exterior, thus producing no sharp edges. Thus, although steel pellets are now widely used, concerns over ricochet and possible accidental harm to bystanders persist (see [1–5]). This paper focuses on modeling of the impact of pellets with a surface and the post-impact ranges (Figure 2) utilizing a discrete element method (DEM) approach, which is ideally suited to the analysis of shotgun pellets. The method's usage has become widespread for physical systems where particles represent a physical unit in granular media, particulate flows, plasmas, swarms, etc.

Corresponding author:
Tarek I. Zohdi, Department of Mechanical Engineering, University of California, 6117 Etchverry Hall, Berkeley, CA 94720-1740, USA.
Email: zohdi@me.berkeley.edu

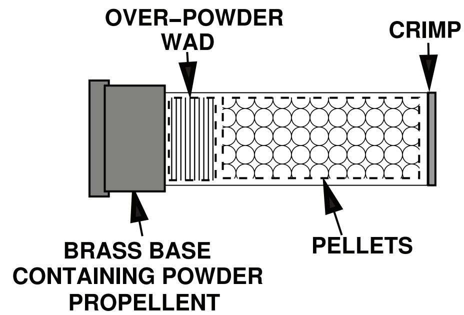

Figure 1. A typical shotgun shell. Depending on the gauge and pellet sizes, there are approximately between 100 and 450 pellets. Diameters of pellets range from 0.00203 to 0.00559 m.

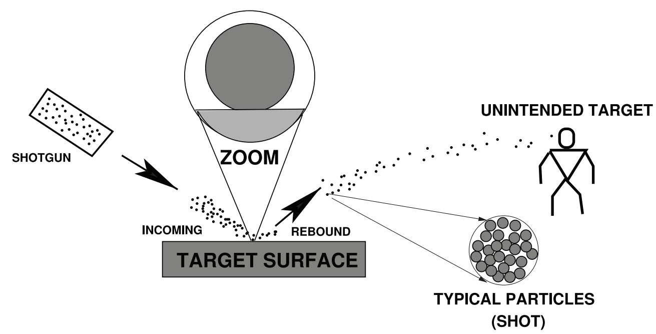

Figure 2. Schematic of a shotgun blast impinging on a target surface and potential rebound with unintended surfaces.

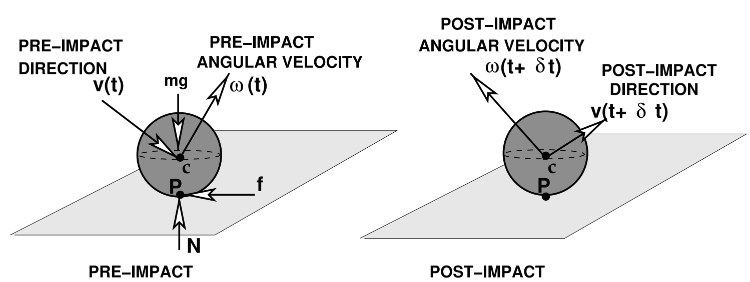

Figure 3. A three-dimensional view of an inelastic pre-impact and post-impact of a pellet on a surface.

Remark 1. Physically, a shotgun blast is similar to the physical process of shot-peening in manufacturing, whose objective is to induce compressive inelastic stresses in the surface of industrial components, such as turbine blades, gears, and cam shafts, in order to suppress failure mechanisms, which are usually driven by tensile stresses, such as crack propagation and fatigue. While this topic is outside of the scope of this paper, we refer the interested reader to [6–10] for the finite-element analysis of the response of the substrate of a shot-peened solid and recently to [11] for rapid computation of multiple contacting bodies on substrates for additive manufacturing processes.

2. Frictional impact model

We formulate a three-dimensional impact scenario as shown in Figure 3. The formulation is capable of describing impact cases of a pellet also with incoming spin, although it is usually minimal in the pre-impact state. We assume that the target surface, which is massive relative to the pellet, does not move.

The impulse in the normal direction for the center of mass, located at point c, is governed by a balance of linear momentum in the normal ($\boldsymbol{e}_n$) direction[2]

$$mv_{c,n}(t) + (N - mg)\delta t = mv_{c,n}(t + \delta t) \Rightarrow N = m\frac{\big(v_{c,n}(t + \delta t) - v_{c,n}(t)\big)}{\delta t} + mg, \tag{1}$$

where m is the mass of the pellet, $v_{c,n}(t)$ is the normal component of the velocity of point c before impact, N is the normal contact force, δt is the impact duration time, g is gravity (assumed in the direction of the normal), and $v_{c,n}(t+\delta t)$ is the normal component of the velocity of point c after impact. A balance of momentum along the direction of the induced friction force provides a means by which one can compute the friction force

$$mv_{c,t}(t) + f\delta t = mv_{c,t}(t+\delta t) \Rightarrow f = m\frac{\left(v_{c,t}(t+\delta t) - v_{c,t}(t)\right)}{\delta t}, \tag{2}$$

where $v_{c,t}(t)$ is the tangential component of the velocity of point c before impact, f is the friction contact force and $v_{c,t}(t+\delta t)$ is the tangential component of the velocity of point c after impact. The direction of the line of action is given by the initial relative tangential velocity at point p

$$\boldsymbol{e}_t = \frac{\boldsymbol{v}_{p,t}(t)}{\|\boldsymbol{v}_{p,t}(t)\|}, \tag{3}$$

where the tangential velocity of the pellet is

$$\boldsymbol{v}_{p,t}(t) = \boldsymbol{v}_p(t) - (\boldsymbol{v}_p(t)\cdot\boldsymbol{e}_n(t))\boldsymbol{e}_n. \tag{4}$$

We note that $\boldsymbol{e}_n$ is invariant for a sphere and plane, and we assume that $\boldsymbol{e}_t$ is the tangent vector during the impact event. If the pellet slips, then direction of friction is

$$\boldsymbol{f} = -f\boldsymbol{e}_t. \tag{5}$$

The velocities of points c and p are related by

$$\boldsymbol{v}_c = \boldsymbol{v}_p + \boldsymbol{\omega}\times\boldsymbol{r}_{p\to c} \Rightarrow \boldsymbol{v}_p = \boldsymbol{v}_c + \boldsymbol{\omega}\times\boldsymbol{r}_{c\to p}, \tag{6}$$

where $\|\boldsymbol{r}_{p\to c}\| = \|\boldsymbol{r}_{c\to p}\| = R$ is the sphere radius. We employ a normal coefficient of restitution that provides information on the velocities of surfaces before and after impact, in the normal direction between the contact point p and the surface[3]:

$$\mathcal{E} = \frac{v_{p,n}(t+\delta t) - 0}{0 - v_{p,n}(t)}, \tag{7}$$

where $0 \le \mathcal{E} \le 1$. Thus,

$$v_{p,n}(t+\delta t) = -\mathcal{E}v_{p,n}(t). \tag{8}$$

In addition, the normal components of p and c are related by

$$v_{p,n} = \boldsymbol{v}_p\cdot\boldsymbol{e}_n = (\boldsymbol{v}_c + \boldsymbol{\omega}\times\boldsymbol{r}_{c\to p})\cdot\boldsymbol{e}_n = v_{c,n}, \tag{9}$$

where $\boldsymbol{e}_n$ is the unit vector in the normal direction. Thus, $v_{c,n}(t+\delta t) = v_{p,n}(t+\delta t)$ and the normal force becomes

$$N = m\frac{v_{c,n}(t+\delta t) - v_{c,n}(t)}{\delta t} + mg = -mv_{c,n}(t)\frac{(1+\mathcal{E})}{\delta t} + mg. \tag{10}$$

The tangential components are related by

$$v_{p,t} = \boldsymbol{v}_p\cdot\boldsymbol{e}_t = (\boldsymbol{v}_c + \boldsymbol{\omega}\times\boldsymbol{r}_{c\to p})\cdot\boldsymbol{e}_t = v_{c,t} + (\boldsymbol{\omega}\times\boldsymbol{r}_{c\to p})\cdot\boldsymbol{e}_t \tag{11}$$

where $\boldsymbol{e}_t$ is the unit vector in the tangential direction. Thus,

$$v_{c,t}(t+\delta t) = v_{p,t}(t+\delta t) - (\boldsymbol{\omega}(t+\delta t)\times\boldsymbol{r}_{c\to p})\cdot\boldsymbol{e}_t. \tag{12}$$

An orthogonal direction to the plane of normal and friction forces is given by

$$\boldsymbol{e}_o = \boldsymbol{e}_t\times\boldsymbol{e}_n \tag{13}$$

and because there are no forces acting in that direction during impact, the velocity components in that direction remain unchanged

$$\boldsymbol{v}_c(t)\cdot\boldsymbol{e}_o = \boldsymbol{v}_c(t+\delta t)\cdot\boldsymbol{e}_o. \tag{14}$$

The total velocity of point c is given by summing the velocities in the three orthogonal directions

$$\boldsymbol{v}_c(t+\delta t) = v_{c,t}(t+\delta t)\boldsymbol{e}_t + v_{c,n}(t+\delta t)\boldsymbol{e}_n + v_{c,o}(t+\delta t)\boldsymbol{e}_o. \tag{15}$$

2.1. Stick–slip friction

Using the preceding relations, the friction force is thus given by

$$f = m\left(\frac{\left(v_{p,t}(t+\delta t) - (\boldsymbol{\omega}(t+\delta t)\times \boldsymbol{r}_{c\to p})\cdot \boldsymbol{e}_t\right) - v_{c,t}(t)}{\delta t}\right). \tag{16}$$

Computing the angular momentum about point c, yields $\boldsymbol{\omega}(t+\delta t)$

$$\bar{\boldsymbol{I}}\cdot\boldsymbol{\omega}(t) + \boldsymbol{r}_{c\to p}\times \boldsymbol{f}\delta t = \bar{\boldsymbol{I}}\cdot\boldsymbol{\omega}(t+\delta t) \Rightarrow \boldsymbol{\omega}(t+\delta t) = \boldsymbol{\omega}(t) + \frac{(\boldsymbol{r}_{c\to p}\times \boldsymbol{f})\delta t}{\bar{I}}, \tag{17}$$

where $\bar{\boldsymbol{I}} = \bar{I}\mathbf{1}$, where $\bar{I} = \frac{2}{5}mR^2$ for a solid sphere. Substituting Equation (16) into Equation (17) yields the following for the friction force

$$f = -\frac{m\bar{I}}{\delta t(\bar{I}+mR^2)}\left(v_{p,t}(t+\delta t) - (\boldsymbol{\omega}(t)\times \boldsymbol{r}_{c\to p})\cdot \boldsymbol{e}_t - v_{c,t}(t)\right). \tag{18}$$

We must subsequently check two cases: (1) tangential stick and (2) possible slip.

2.2. Case 1: no tangential slip

If we assume no tangential slip, thus $v_{pt}(t+\delta t) = 0$, leading to

$$f = \frac{m\bar{I}}{\delta t(\bar{I}+mR^2)}\left((\boldsymbol{\omega}(t)\times \boldsymbol{r}_{c\to p})\cdot \boldsymbol{e}_t + v_{c,t}(t)\right), \tag{19}$$

where $N = -\dfrac{mv_{c,n}(t)}{\delta t}(1+\mathcal{E}) + mg$, where

$$\boldsymbol{\omega}(t+\delta t) = \boldsymbol{\omega}(t) + \frac{(\boldsymbol{r}_{c\to p}\times \boldsymbol{f})\delta t}{\bar{I}} = \boldsymbol{\omega}(t) - \frac{fR\delta t}{\bar{I}}\boldsymbol{e}_o, \tag{20}$$

and

$$v_{c,t}(t+\delta t) = v_{c,t}(t) - \frac{f\delta t}{m} \tag{21}$$

Slipping occurs if the Coulomb friction limit is exceeded.

2.3. Case 2: slipping

If the Coulomb friction limit is exceeded

$$|f| > \mu_s|N|, \tag{22}$$

this implies that the no slip assumption is incorrect, then

$$\boldsymbol{f} = -\mu_d N\boldsymbol{e}_t = \mu_d\left(\frac{m}{\delta t}(1+\mathcal{E})v_{c,n}(t) - mg\right)\boldsymbol{e}_t, \tag{23}$$

where we note that $v_{c,n}(t)$ is negative. Thus,

$$\begin{aligned}\boldsymbol{\omega}(t+\delta t) = \boldsymbol{\omega}(t) + \frac{(\boldsymbol{r}_{c\to p}\times \boldsymbol{f})\delta t}{\bar{I}} &= \boldsymbol{\omega}(t) - \frac{\mu_d NR\delta t}{\bar{I}}\boldsymbol{e}_o \\ &= \boldsymbol{\omega}(t) + \frac{\mu_d\left(m(1+\mathcal{E})v_{c,n}(t) - mg\delta t\right)R}{\bar{I}}\boldsymbol{e}_o,\end{aligned} \tag{24}$$

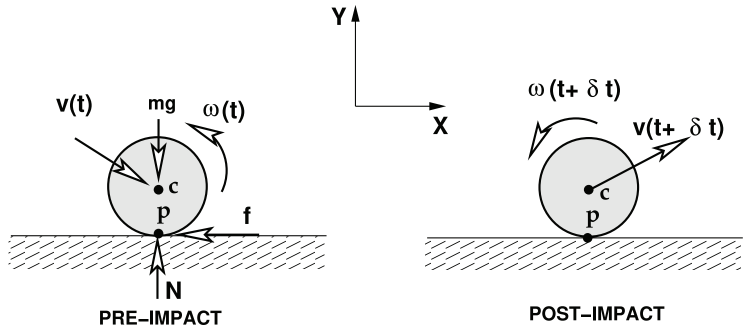

Figure 4. Purely planar impact scenario.

and

$$v_{c,t}(t+\delta t) = v_{c,t}(t) - \frac{f\delta t}{m} = v_{c,t}(t) - \frac{\mu_d N\delta t}{m} = v_{c,t}(t) - \mu_d(1+\mathcal{E})v_{c,n}(t) + \mu_d g\delta t. \tag{25}$$

Remark 2: In order to determine post-impact trajectories one can post-process the post-impact velocity vector and unit vector ($\boldsymbol{d}(t+\delta t)$):

$$\boldsymbol{d}(t+\delta t) \stackrel{\text{def}}{=} \frac{\boldsymbol{v}(t+\delta t)}{||\boldsymbol{v}(t+\delta t)||}. \tag{26}$$

We also note that the time-averaged impulses are $N^* \stackrel{\text{def}}{=} N\delta t$ and $f^* \stackrel{\text{def}}{=} f\delta t$ are independent of δt.

2.4. *Special case: purely planar (two-dimensional) impact*

More insight can be obtained from considering the special case of purely planar impact (Figure 4), with $\omega(t) = \omega(t)\boldsymbol{e}_o$.

Case 1: no tangential slip. If we assume no tangential slip, thus $v_{pt}(t+\delta t) = 0$, leading to

$$f = \frac{m\bar{I}}{\delta t(\bar{I} + mR^2)}\left(\omega(t)R + v_{c,t}(t)\right), \tag{27}$$

where $N = -\frac{mv_{c,n}(t)}{\delta t}(1+\mathcal{E}) + mg$, and

$$\omega(t+\delta t) = \omega(t) - \left(\frac{mR}{\bar{I} + mR^2}\right)\left(\omega(t)R + v_{c,t}(t)\right) \tag{28}$$

and

$$v_{c,t}(t+\delta t) = v_{c,t}(t) - \left(\frac{\bar{I}}{\bar{I} + mR^2}\right)\left(\omega(t)R + v_{c,t}(t)\right) \tag{29}$$

and, as previously,

$$v_{c,n}(t+\delta t) = -\mathcal{E}v_{c,n}(t). \tag{30}$$

2.5. *Case 2: slipping*

As previously, if the Coulomb friction limit is exceeded, this implies that the no slip assumption is incorrect, then friction acts in the opposite $\boldsymbol{e}_t$ direction with magnitude

$$f = \mu_d N = -\frac{m\mu_d}{\delta t}(1+\mathcal{E})v_{c,n}(t) + \mu_d mg, \tag{31}$$

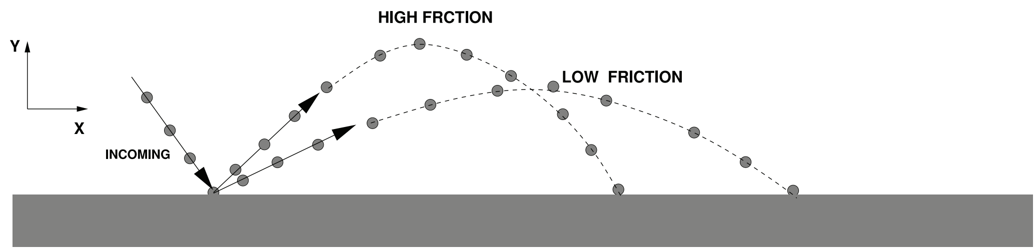

Figure 5. Impact trajectories for a single pellet with varying friction.

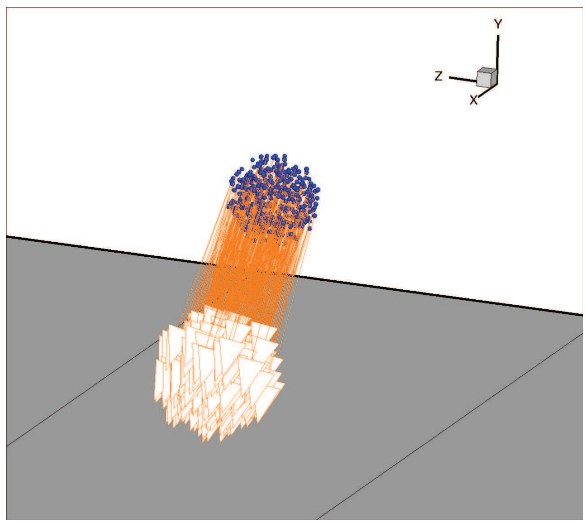

Figure 6. Starting configuration of the pellets. See Figure 7 for the impact sequence.

where we note that $v_{c,n}(t)$ is negative, and

$$\omega(t+\delta t)=\omega(t)+\frac{(m\mu_d(1+\mathcal{E})v_{c,n}(t)-mg\delta t)R}{\bar{I}}, \tag{32}$$

and

$$v_{c,t}(t+\delta t)=v_{c,t}(t)-\frac{\mu_d N\delta t}{m}=v_{c,t}(t)-\mu_d(1+\mathcal{E})v_{c,n}(t)+\mu_d g\delta t \tag{33}$$

and, as previously,

$$v_{c,n}(t+\delta t)=-\mathcal{E}v_{c,n}(t). \tag{34}$$

Remark 3: In either case, the trajectory of the post-impact angle is

$$\theta(t+\delta t)=\tan^{-1}\left(\frac{v_{c,n}(t+\delta t)}{v_{c,t}(t+\delta t)}\right), \tag{35}$$

and because $v_{c,t}(t+\delta t)$ will generally decrease for greater friction, a more vertical trajectory occurs, however, with less translational energy. A schematic of the expected differences in the trajectory of a post-impact pellet with varying friction are depicted in Figure 5.

3. Three-dimensional multi-pellet impact study

3.1. System parameters

The following system parameters are considered, corresponding closely to those of a small-scale shotgun pellet.

- A total of 450 pellets in the system (normal 12-gauge shotgun shells have between approximately 100 and 450 pellets).

- Pellet diameter: $D = 2R = 0.0025$ m (typical pellets ranges from 0.00203 and 0.00559 m).
- Incoming distribution of pellets within a starting radius spherical envelope (Figure 6): $R^e = 0.025$ m.
- Density of pellets: $\rho = 7000$ kg/m^3, thus the mass is $m_p = \rho\frac{4}{3}\pi R^3$.
- Initial pellet velocities: $\boldsymbol{v}_o = (v_{xo}, v_{yo}, v_{zo})$, where $\|\boldsymbol{v}_o\| = 1350$ft/s $= 411.46$ m/s.
- Initial pellet directions: $\boldsymbol{n} = \dfrac{\boldsymbol{d}}{\|\boldsymbol{d}\|}$, $\boldsymbol{d} = (1 \pm 0.1, -1 \pm 0.1, 0 \pm 0.1)$.
- Initial pellet angular velocities (zero): $\boldsymbol{\omega} = (\omega_{xo}, \omega_{yo}, \omega_{zo}) = (0, 0, 0)$ rad/s.
- Normal coefficient of restitution (appropriate for steel on hard plastic): $\mathcal{E} = 0.01$.

We vary the key system parameter, namely the static friction coefficient, in the range $0 \leq \mu_s \leq 0.5$ and the corresponding dynamic friction coefficient as $\mu_d = 0.9\mu_s$. The following quantities are important.

- Pre-impact ensemble tangential velocity: $\langle v_{c,t}(t)\rangle_N \stackrel{\text{def}}{=} \frac{1}{N}\sum_{i=1}^{N} v_{c,t,i}(t)$.
- Post-impact ensemble tangential velocity: $\langle v_{c,t}(t+\delta t)\rangle_N \stackrel{\text{def}}{=} \frac{1}{N}\sum_{i=1}^{N} v_{c,t,i}(t+\delta t)$.
- Pre-impact ensemble normal velocity: $\langle v_{c,n,i}(t)\rangle_N \stackrel{\text{def}}{=} \frac{1}{N}\sum_{i=1}^{N} v_{c,n,i}(t)$.
- Post-impact ensemble normal velocity: $\langle v_{c,n,i}(t+\delta t)\rangle_N \stackrel{\text{def}}{=} \frac{1}{N}\sum_{i=1}^{N} v_{c,n,i}(t+\delta t)$.
- Pre-impact ensemble normal translational energies: $\langle W_{T,i}(t)\rangle_N \stackrel{\text{def}}{=} \frac{1}{N}\sum_{i=1}^{N} \frac{1}{2}m_i\boldsymbol{v}_i(t)\cdot\boldsymbol{v}_i(t)$.
- Post-impact ensemble normal translational energies: $\langle W_{T,i}(t+\delta t)\rangle_N \stackrel{\text{def}}{=} \frac{1}{N}\sum_{i=1}^{N} \frac{1}{2}m_i\boldsymbol{v}_i(t+\delta t)\cdot\boldsymbol{v}_i(t+\delta t)$.
- Pre-impact ensemble rotational energies: $\langle W_{R,i}(t)\rangle_N \stackrel{\text{def}}{=} \frac{1}{N}\sum_{i=1}^{N} \frac{1}{2}\boldsymbol{\omega}_i(t)\cdot\bar{\boldsymbol{I}}_i\cdot\boldsymbol{\omega}_i(t)$.
- Post-impact ensemble rotational energies: $\langle W_{R,i}(t+\delta t)\rangle_N \stackrel{\text{def}}{=} \frac{1}{N}\sum_{i=1}^{N} \frac{1}{2}\boldsymbol{\omega}_i(t+\delta t)\cdot\bar{\boldsymbol{I}}_i\cdot\boldsymbol{\omega}_i(t+\delta t)$.
- Ratios of post-impact and pre-impact ensemble energies: $\dfrac{W_{T,i}(t)+W_{R,i}(t)}{W_{T,i}(t+\delta t)+W_{R,i}(t+\delta t)}$.

As Tables 1–3 illustrate, with decreasing friction the trajectory decreases (shallower rebound relative to the impact plane) and the pre-impact and post-impact translational and rotational kinetic energies. Above a friction coefficient of $\mu_s = 0.1$, the pellets in the system uniformly stick. The subsequent post-impact spin is also substantial owing to the "jolt" from friction, combined with the fact that the pellets are small. In the high-friction cases $\mu_s > 0.1$, significantly more translational kinetic energy is converted into rotational energy. When slipping occurs, then a significant amount of translational energy is retained in the post-impact stage, and the ranges of the pellets will be much greater, as shown next.

3.2. *Post-impact trajectories-projectile travel*

Post-impact computational of the pellets are shown in Figures 6 and 7. The position of a pellet is given by

$$\boldsymbol{r}(t) = \boldsymbol{r}(t=0) + \boldsymbol{v}(t=0) + \frac{1}{2}\boldsymbol{g}t^2. \tag{36}$$

In the special case of $\boldsymbol{g} = (0, -g, 0)$, we have for the first $(x_1 = x)$ component, which is parallel to the plane of contact:

$$r_1(t) = r_1(0) + v_1(0)t \tag{37}$$

and for the $(x_2 = y)$ component, which is perpendicular to the plane of contact (aligned with gravity)

$$r_2(t) = r_2(0) + v_2(t=0)t - \frac{1}{2}gt^2 \tag{38}$$

and for the third $(x_3 = z)$ component which is parallel to the plane of contact:

$$r_3(t) = r_3(0) + v_3(0)t. \tag{39}$$

The time aloft after impact is determined by computing the time to reach the peak of $r_2(t)$ (normal direction) and to return to ground:

$$t^* = \sqrt{\frac{2v_2(0)}{g}} + \sqrt{\frac{2v_2(0)}{g}} = 2\sqrt{\frac{2v_2(0)}{g}}. \tag{40}$$

Table 1. Pre- and post-impact velocities.

μ_s	Time	$\langle v_{c,t}\rangle_N$ (m/s)	$\langle v_{c,n}\rangle_N$ (m/s)	$\|\langle \boldsymbol{\omega}\rangle_N\|$ (rad/s)
0.500	0.000	290.454	−290.959	0.000
0.500	0.010	36.950	2.892	29,880.239
0.450	0.000	290.454	−290.959	0.000
0.450	0.010	36.950	2.892	29,880.239
0.400	0.000	290.454	−290.959	0.000
0.400	0.010	36.950	2.892	29,880.239
0.350	0.000	290.454	−290.959	0.000
0.350	0.010	36.950	2.892	29,880.239
0.300	0.000	290.454	−290.959	0.000
0.300	0.010	36.950	2.892	29,880.239
0.250	0.000	290.454	−290.959	0.000
0.250	0.010	36.950	2.892	29,880.239
0.200	0.000	290.454	−290.959	0.000
0.200	0.010	36.950	2.892	29,880.239
0.150	0.000	290.454	−290.959	0.000
0.150	0.010	36.950	2.892	29,880.239
0.100	0.000	290.454	−290.959	0.000
0.100	0.010	36.950	2.892	29,880.239
0.050	0.000	290.454	−290.959	0.000
0.050	0.010	158.212	2.892	26,223.662
0.000	0.000	290.454	−290.959	0.000
0.000	0.010	290.454	2.892	0.000

In the tangential plane of impact ($v_t = \sqrt{v_1^2 + v_3^2}$)

$$r_t(t^*) = r_t(0) + v_t(0)t^*. \tag{41}$$

The radius of spread is given by

$$L = r_t(t^*) - r_t(0) = v_t(0)t^* = 2\sqrt{(v_1(0)^2 + v_3(0)^2)\frac{2v_2(0)}{g}}. \tag{42}$$

For the distribution of the pellets in a blast, with increasingly less friction, we see that the second to last parameter group (Tables 1–3, $\mu_s = 0.05$) exhibits partial slip, and the final parameter group ($\mu_s = 0.0$) exhibits complete slip. The distribution of the pellets within each regime is due to the initial directional distribution ($\boldsymbol{d}$) in the pre-impact blast envelope. Tabulated are $L^- \leq Range = L \leq L^+$ and the ensemble average is $\langle L\rangle_N \stackrel{\text{def}}{=} \frac{1}{N}\sum_{i=1}^{N} L_i$. When there is no slip, the variation of the spread of pellets in between 17.00 m $\leq L \leq$ 21.88 m, which for the transitional stick–slip system it is 17.00 m $\leq L \leq$ 164.91 m and for the complete slip system 169.30 m $\leq L \leq$ 172.58 m and for the complete slip system. The two key trends are as follows.

- For increasing friction, translational energy gets converted to rotational energy and consequently provides less post-impact energy available for translational motion.
- For increasing friction, the trajectory is steeper, but because of less post-impact energy available for translational motion, the range of ricochet is significantly smaller than cases where slipping occurs.

4. Summary

The present work has focused on the building block of a shotgun blast, namely the oblique inelastic impact of a pellet with a frictional surface. The governing equations for a general three-dimensional inelastic impact with

Table 2. Spin and translational and rotational kinetic energies.

μ_s	Time	$\langle W_T\rangle_N$ μ (J)	$\langle W_R\rangle_N$ μ (J)	$\frac{\langle W_T\rangle_N}{\langle W(t=0)\rangle_N}$	$\frac{\langle W_R\rangle_N}{\langle W(t=0)\rangle_N}$
0.500	0.000	4.843	0.000	1.000	0.000
0.500	0.010	0.039	0.015	0.008	0.003
0.450	0.000	4.843	0.000	1.000	0.000
0.450	0.010	0.039	0.015	0.008	0.003
0.400	0.000	4.843	0.000	1.000	0.000
0.400	0.010	0.039	0.015	0.008	0.003
0.350	0.000	4.843	0.000	1.000	0.000
0.350	0.010	0.039	0.015	0.008	0.003
0.300	0.000	4.843	0.000	1.000	0.000
0.300	0.010	0.039	0.015	0.008	0.003
0.250	0.000	4.843	0.000	1.000	0.000
0.250	0.010	0.039	0.015	0.008	0.003
0.200	0.000	4.843	0.000	1.000	0.000
0.200	0.010	0.039	0.015	0.008	0.003
0.150	0.000	4.843	0.000	1.000	0.000
0.150	0.010	0.039	0.015	0.008	0.003
0.100	0.000	4.843	0.000	1.000	0.000
0.100	0.010	0.039	0.015	0.008	0.003
0.050	0.000	4.843	0.000	1.000	0.000
0.050	0.010	1.040	0.012	0.215	0.002
0.000	0.000	4.843	0.000	1.000	0.000
0.000	0.010	2.419	0.000	0.499	0.000

Table 3. Post-impact ricochet ranges.

μ_s	$\langle L\rangle_N$ (m)	L^+ (m)	L^- (m)	Frictional case
0.500	21.888	27.595	17.001	All-stick
0.450	21.888	27.595	17.001	All-stick
0.400	21.888	27.595	17.001	All-stick
0.350	21.888	27.595	17.001	All-stick
0.300	21.888	27.595	17.001	All-stick
0.250	21.888	27.595	17.001	All-stick
0.200	21.888	27.595	17.001	All-stick
0.150	21.888	27.595	17.001	All-stick
0.100	21.888	27.595	17.001	All-stick
0.050	92.908	164.918	17.001	Mixed: stick+slip
0.000	172.016	172.584	169.308	All-slip

unilateral stick–slip conditions were derived, with the objective being to determine the relationship between pre-impact and post-impact pellet trajectories and the post-impact range of travel. The analysis is useful to researchers interested in ascertaining the potential danger in from ricochet in shotgun blasts. In this work, it was implicitly assumed that the pellets do not collide with each other during the entire process. Investigation of the degree of error introduced by this simplifying assumption is under current investigation by the author. Specifically, the current work of the author is focused on more detailed impact analyses coupling multi-pellet impact to the plastic deformation and damage of the impacted surface, utilizing DEM formulations for multiple bodies in simultaneous contact, such as those found in [12–27].

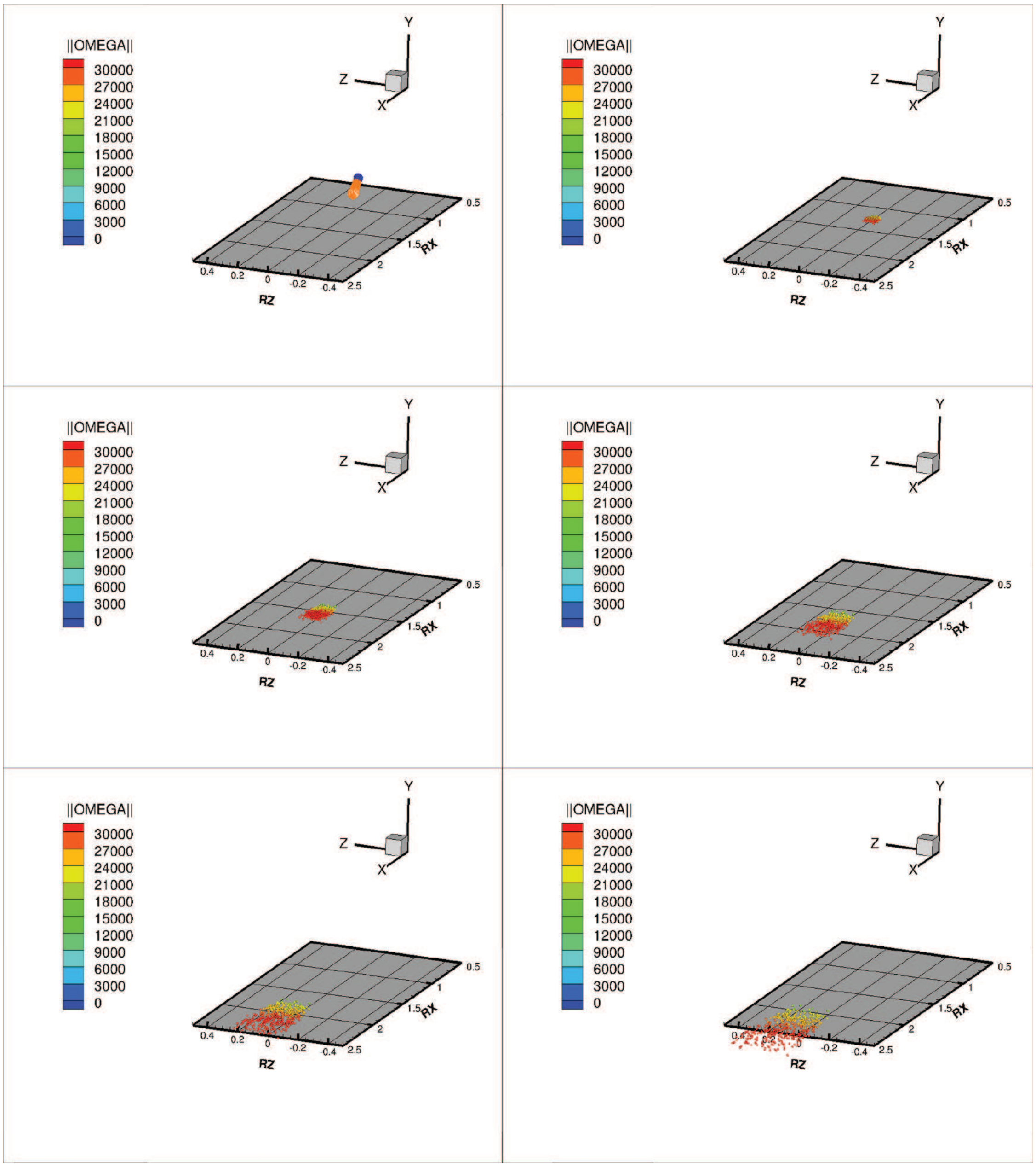

Figure 7. Top to bottom and left to right: Sequential impact trajectories for $\mu_s = 0.5$ for 450 pellets. The colors indicate the norm of the angular velocities.

Funding

This research received no specific grant from any funding agency in the public, commercial, or not-for-profit sectors.

ORCID iD

Tarek I. Zohdi https://orcid.org/0000-0002-0844-3573

Notes

1. In a 12-gauge shotgun shell, there are approximately between 100 and 450 pellets, with pellet diameters ranging from 0.00203 to 0.00559 m.
2. We ignore any aerodynamic effects, such as drag and the Magnus effect, whereby a spinning pellet with angular velocity $\boldsymbol{\omega}$ and velocity $\boldsymbol{v}_c$ creates unequal drag forces on the surface, because the points on the surface are traveling at unequal absolute speeds ($\boldsymbol{v}_p = \boldsymbol{v}_c + \boldsymbol{\omega} \times \boldsymbol{r}_{c \to p}$). We concentrate only on the instants directly before and after the impact event itself.
3. If we assumed that the surface's velocity was zero, we would obtain $v_{p,n}(t + \delta t) = -v_{p,n}(t)\mathcal{E}$.

References

[1] Centers for Disease Control and Prevention. Web-based Injury Statistics Query and Reporting System (WISQARS). Atlanta, GA: National Center for Injury Prevention and Control, 2019. Available at: http://www.cdc.gov/injury/wisqars/index.html (accessed: 10 April 2021).

[2] Fowler, K, Dahlberg, LL, Haileyesus, T, Annest, JL, and Bacon, S. Firearm injuries in the United States. *Prevent Med* 2015; 79: 5–14.

[3] Ivey-Stephenson, AZ, Crosby, AE, Jack, SP, Haileyesus, T, and Kresnow-Sedacca, M. Suicide trends among and within urbanization levels by sex, race/ethnicity, age group, and mechanism of death - United States, 2001–2015. *MMWR Surveill Sum* 2017; 66(No. SS-18): 1–16.

[4] Kann, L, McManus, T, Harris, WA, et al. Youth risk behavior surveillance - United States, 2017. *MMWR Surveill Sum* 2018; 67(No. SS-8): 1–114.

[5] National Research Council. *Priorities for Research to Reduce the Threat of Firearm-related Violence*. Washington, DC: National Academies Press, 2013.

[6] Afazov, SM, Becker, AA, and Hyde, TH. Mathematical modeling and implementation of residual stress mapping from microscale to macroscale finite element models. *J Manuf Sci Eng* 2012; 134(2): 021001.

[7] Bagherifard, S, Giglio, M, Giudici, L, and Guagliano, M. Experimental and numerical analysis of fatigue properties improvement in a titanium alloy by shot peening. In: *ASME 2010 10th Biennial Conference on Engineering Systems Design and Analysis*, Vol. 2 (*Proc ASME* 49163), 2010, pp. 317–322.

[8] Elbella, A, Fadul, F, Uddanda, SH, and Kasarla, NR. Influence of shot peening parameters on process effectiveness. In: *ASME 2012 International Mechanical Engineering Congress and Exposition. Volume 3: Design, Materials and Manufacturing, Parts A, B, and C* (*Proc ASME* 45196), 2013, pp. 2015–2021.

[9] Chen, Z, Yang, F, and Meguid, SA. Realistic finite element simulations of arc-height development in shot-peened Almen strips. *J Eng Mater Technol* 2014; 136(4): 041002.

[10] Wriggers, P. *Computational Contact Mechanics*. New York: John Wiley & Sons, Inc., 2002.

[11] Zohdi, TI. *Modeling and Simulation of Functionalized Materials for Additive Manufacturing and 3D Printing: Continuous and Discrete Media*. Berlin: Springer-Verlag, 2018.

[12] Duran, J. *Sands, Powders and Grains. An Introduction to the Physics of Granular Matter.* Berlin: Springer-Verlag, 1997.

[13] Pöschel, T, and Schwager, T. *Computational Granular Dynamics*. Berlin: Springer-Verlag, 2004.

[14] Onate, E, Idelsohn, SR, Celigueta, MA, and Rossi, R. Advances in the particle finite element method for the analysis of fluid–multibody interaction and bed erosion in free surface flows. *Comput Meth Appl Mech Eng* 2008; 197(19–20): 1777–1800.

[15] Onate, E, Celigueta, MA, Idelsohn, SR, Salazar, F, and Suárez, B. Possibilities of the particle finite element method for fluid–soil–structure interaction problems. *Computat Mech* 2011; 48: 307–318.

[16] Carbonell, JM, Onate, E, and Suarez, B. Modeling of ground excavation with the particle finite element method. *J Eng Mech* 2010; 136: 455–463.

[17] Labra, C, and Onate, E. High-density sphere packing for discrete element method simulations. *Commun Numer Meth Eng* 2009; 25(7): 837–849.

[18] Rojek, J, Labra, C, Su, O, and Onate, E. Comparative study of different discrete element models and evaluation of equivalent micromechanical parameters. *Int J Solids Struct* 2012; 49: 1497–1517.

[19] Rojek, J. Discrete element thermomechanical modelling of rock cutting with valuation of tool wear. *Computat Particle Mech* 2014; 1(1): 71–84.

[20] Onate, E, Celigueta, MA, Latorre, S, Casas, G, Rossi, R, and Rojek, J. Lagrangian analysis of multiscale particulate flows with the particle finite element method. *Computat Particle Mech* 2014; 1(1): 85–102.

[21] Leonardi, A, Wittel, FK, Mendoza, M, and Herrmann, HJ. Coupled DEM-LBM method for the free-surface simulation of heterogeneous suspensions. *Computat Particle Mech* 2014; 1(1): 3–13.

[22] Cante, J, Davalos, C, Hernandez, JA, et al. PFEM-based modeling of industrial granular flows. *Computat Particle Mech* 2014; 1(1): 47–70.

[23] Bolintineanu, DS, Grest, GS, Lechman, JB, Pierce, F, Plimpton, SJ, and Schunk, PR. Particle dynamics modeling methods for colloid suspensions. *Computat Particle Mech* 2014; 1(3): 321–356.

[24] Avci, B, and Wriggers, P. A DEM-FEM coupling approach for the direct numerical simulation of 3D particulate flows. *J Appl Mech* 2012; 79: 010901.

[25] Zohdi, TI. A direct particle-based computational framework for electrically-enhanced thermo-mechanical sintering of powdered materials. *Math Mech Solids* 2014; 19(1): 93–113.
[26] Zohdi, TI. Additive particle deposition and selective laser processing-a computational manufacturing framework. *Computat Mech* 2014; 54: 171–191.
[27] Zohdi, TI. Modeling and efficient simulation of the deposition of particulate flows onto compliant substrates. *Int J Eng Sci* 2015; 99: 74–91.